

Modeling an efficient singlet-triplet-spin-qubit-to-photon interface assisted by a photonic crystal cavity

Kui Wu^{1,*†}, Sebastian Kindel^{1,‡}, Thomas Descamps^{1,§}, Tobias Hangleiter^{1,§}, Jan Christoph Müller,² Rebecca Rodrigo,¹ Florian Merget,¹ Beata E. Kardynal^{1,§,4}, Hendrik Bluhm^{1,§,5} and Jeremy Witzens¹

¹ Institute of Integrated Photonics, RWTH Aachen University, Aachen 52074, Germany

² JARA-FIT Institute for Quantum Information, Forschungszentrum Jülich GmbH and RWTH Aachen University, Aachen 52074, Germany

³ Peter Grünberg Institute, Forschungszentrum Jülich GmbH, Jülich 52425, Germany

⁴ Department of Physics, RWTH Aachen University, Aachen 52074, Germany

⁵ ARQUE Systems GmbH, Aachen 52074, Germany



(Received 23 October 2023; revised 26 March 2024; accepted 3 May 2024; published 24 May 2024)

Efficient interconnection between distant semiconductor spin qubits with the help of photonic qubits offers exciting new prospects for future quantum communication applications. In this paper, we optimize the extraction efficiency of a novel interface between a singlet-triplet-spin-qubit and a photonic-qubit. The interface is based on a 220-nm-thick GaAs/(Al,Ga)As heterostructure membrane and consists of a gate-defined double quantum dot (GDQD) supporting a singlet-triplet qubit, an optically active quantum dot (OAQD) consisting of a gate-defined exciton trap, a photonic crystal cavity providing in-plane optical confinement, efficient outcoupling to an ideal free-space Gaussian beam while accommodating the gate wiring of the GDQD and OAQD, and a bottom gold reflector to recycle photons and increase the optical extraction efficiency. All the essential components can be lithographically defined and deterministically fabricated on the GaAs/(Al,Ga)As heterostructure membrane, which greatly increases the scalability of on-chip integration. According to our simulations, the interface provides an overall coupling efficiency of 28.7% into a free-space Gaussian beam, assuming a SiO₂ interlayer fills the space between the reflector and the membrane. The performance can be further increased by undercutting this SiO₂ interlayer below the photonic crystal. In this case, the overall efficiency is calculated to be 48.5%.

DOI: 10.1103/PhysRevApplied.21.054052

I. INTRODUCTION

Interconnecting distant stationary qubits with photonic qubits is a pivotal milestone for the quantum Internet [1], where quantum entanglement is distributed between different quantum technology platforms to enable specialized quantum information applications, such as physically secured quantum communication [2,3] and distributed quantum computation [4]. Among the competing qubit hardware platforms, gate-defined double quantum dots (GDQDs) offer promising prospects due to their compatibility with standard top-down fabrication techniques and the potential for integrating multiple locally interconnected qubits. In a GDQD, single electrons are trapped by tunable electrostatic potential minima applied to a two-dimensional electron gas (2DEG) with surface metal gates. Moreover, singlet-triplet spin qubits defined by GDQDs

enable all electrical control via the exchange interaction and high-speed (tens of nanoseconds) manipulation of qubit states [5,6]. Likewise, the subnanosecond scale recombination time enables a high emission rate and offers a potential for high optical efficiency even without Purcell enhancement, which is an advantage over other platforms like nitrogen-vacancy centers in diamonds [7–10] and ion traps [11].

GDQD qubits based on gallium arsenide (GaAs) have demonstrated all the key prerequisites for quantum information applications, including qubit initialization, readout, and coherent control [5,6,12–15]. Although spin qubits based on isotope-purified ²⁸Si platforms exhibit a much longer coherence time [16,17], the indirect bandgap of Si is not suitable for light emission and, thus, presents an obstacle when implementing an optical interface between spin qubits and photonic qubits. On the other hand, the direct bandgap of GaAs offers a path toward photonic-qubit to spin-qubit conversion, making it an attractive material for the objectives pursued here. In the longer term,

*kwu@iph.rwth-aachen.de

†These authors have contributed equally to this paper.

the heterogeneous integration of III–V quantum dots on silicon quantum circuits holds promise [18] for combining the optimal properties of both materials.

Coherent interfacing between photonic qubits and spin qubits on GDQD systems remains challenging due to the lack of hole confinement in conventional heterostructures, resulting in a loss of correlated photon information. One possible solution to this issue is integrating an optically active quantum dot (OAQD), for example, an InAs self-assembled quantum dot (SAQD) or a fully gate-defined electrostatic exciton trap [19], as an intermediary between the photonic-qubit and the GDQD-spin-qubit. A transfer protocol [20] is then applied to adiabatically and coherently tunnel-couple the photogenerated electron to a singlet-triplet-spin-qubit in a GDQD. Consequently, the OAQDs need to be placed in close proximity to the GDQD to enable the transfer of the electron via tunneling from one dot to the other. For concreteness, we describe a fully gate-defined design using an electrostatic trap, but this approach can be transferred to other devices in which highly efficient optical coupling to planar semiconductor structures needs to be combined with electrical connectivity, up to roughly micron-scale device sizes. Such an electrostatic exciton trap has the advantage of allowing a fully lithographically defined fabrication process and, thus, enhanced reproducibility and spatial control without compromising the functionality of the transfer protocol. Furthermore, the exciton energy is controllable via the quantum-confined Stark effect (QCSE) and features a narrow spectral linewidth, as shown in earlier demonstrations [19].

Efficient coupling between the OAQD and an optical fiber is a critical aspect of a functional optical interface. Due to the large refractive index contrast between GaAs and free space, photons need to be emitted in a narrow escape cone to be able to couple to a free-space mode, limiting the outcoupling efficiency. Various optical nanostructures, such as micropillar cavities [21], nanowire waveguides [22], microlenses [23–25], and in-plane evanescent coupling [26–28], have been investigated to increase the outcoupling efficiency by up to 80% [27,28]. However, these structures have been designed and measured using SAQDs as single photon sources and need to be adapted or are incompatible with an electrostatic exciton trap. An additional challenge not met by these solutions is the routing of electrical contacts. Thus, there is a demand for an efficient optical interface supporting the integration of GDQDs and gate-defined OAQDs.

Photonic crystal cavities (PCCs) are widely used in quantum nanotechnology experiments due to their ability to enhance light-matter interaction through the well-known Purcell effect. Integrating InAs SAQDs into GaAs photonic crystal structures enables controlled spontaneous emission rates [29,30], high-quality single photon emission [31], strong light-matter interaction [31–33], and high

on-chip source efficiency [34]. Moreover, by carefully adjusting the PCC geometry, cavity modes can be tailored, including wavelength, mode profile, and radiation properties [35,36], to meet application requirements. Given the deterministic fabrication and inherent scalability of planar, two-dimensional geometries, which apply to both GDQDs and photonic crystal structures, integrating them into a single device holds promise. Previous studies have reported enhanced photoluminescence in a PCC [37] and optical absorption in a bullseye cavity [38] fabricated on a GaAs/(Al,Ga)As quantum well membrane with metal electrodes. We have previously reported the design of an H4 photonic crystal cavity with a simplified gate-defined OAQD model, which showed potential for achieving good coupling efficiency to an optical fiber mode [39].

In this paper, we present a comprehensive design of a novel singlet-triplet-spin-qubit to fiber interface that comprises the complete electrode system required to define all the traps as well as a charge sensor. Our approach involves using a gate-defined electrostatic exciton trap as an OAQD, placed at the center of a carefully designed photonic crystal cavity, which allows for electrical contacts to be routed to the GDQD and OAQD. The GDQD, OAQD, and PCC are fully lithographically defined in a 220-nm-thick GaAs/(Al,Ga)As heterostructure membrane supporting a 2DEG. The cavity is designed in such a way that highly efficient vertical emission is achieved at the working wavelength of the OAQD (i.e., 823 nm).

Four cavity openings, which are created by removing and rescaling part of the photonic crystal holes, are incorporated into the cavity to enable electrical connectivity to the surrounding membrane via the 2DEG, as required for the charge sensor and the initialization of the GDQD. Since defect-induced trapped surface charges accumulated on the etched side walls of the holes deplete the surrounding 2DEG, such cavity openings are required to create an electrical channel for electrical transport through the 2DEG. The cavity openings are engineered to feature a mini stopband [40] centered around 823 nm to maintain the optical confinement of the cavity since they would otherwise form photonic crystal waveguides [41] that allow light to leak out.

A gold back-reflector is deposited onto the GaAs/(Al,Ga)As membrane over an intermediate SiO₂ layer to coherently recycle photons emitted toward it and enable unidirectional emission. The entire layer stack (i.e., the GaAs/(Al,Ga)As membrane, SiO₂, and gold reflector) is flipped and transferred to a silicon substrate and attached via epoxy, after which the front side electrodes are fabricated and the PCC is etched. The distance between the reflector and the heterostructure membrane is optimized to ensure that the desired vertical emission is constructively enhanced.

In order to evaluate the performance accurately, we applied rigorous vectorial overlap calculations in this

paper. According to our calculations, this design ensures that more than 50% of the photons emitted by the OAQD are coupled into a narrow free-space beam in the perpendicular direction, which in turn has an optical overlap greater than 50% with an ideal Gaussian beam. This design has a promising potential for enabling efficient and scalable quantum information applications with GDQD and photonic crystal cavity integration.

II. GDQD AND OAQD STRUCTURE

The detailed geometry of the GDQD, OAQD, and a quantum dot charge sensor (also known as a single-electron transistor) is depicted in Fig. 1. The electrodes defining these structures are deposited on a 220-nm GaAs/(Al,Ga)As heterostructure membrane. The electrodes are made of Au/Ti wires with a thickness of 9 nm (i.e., 2-nm-thick Ti and 7-nm-thick Au). The wires of both GDQD and the sensor have a width of 30 nm. The OAQD consists of round guard gates (with an outer diameter of 400 nm) and a central trap gate (central diameter of 116 nm). Electrical voltages are applied to the gates to create local potential minima in the 2DEG in the 20-nm GaAs quantum well, which confine the singlet-triplet-spin-qubit in the GDQD and the exciton under the trap gate of the OAQD. The wires defining the GDQD and the sensor are only patterned on the top side of the membrane following a validated geometry, while those defining the OAQD are deposited symmetrically on both sides of the membrane to ensure a strongly localized electric field and independent tuning of the exciton trap via the QCSE [42].

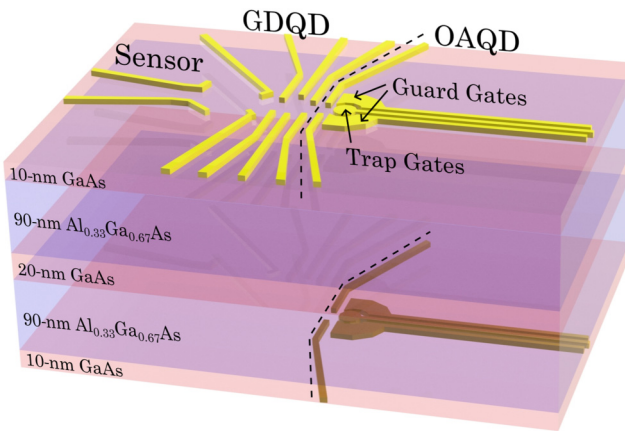


FIG. 1. Schematic view of the gate-defined quantum dot (GDQD), the optically active quantum dot (OAQD), and the quantum dot charge sensor defined on a 220-nm GaAs/(Al,Ga)As heterostructure membrane. The electrodes defining the OAQD are deposited on both sides of the membrane to ensure a strongly localized electric field. On the other hand, the GDQD and the quantum dot charge sensor only require top-side electrodes.

A preliminary design of the gate structures had been published in a conference proceeding [43]. Here, we improve on this work by introducing the finalized gate structure, in which the exciton trap geometry, the GDQD layout, and the tunnel coupling between the exciton trap and the GDQD have been verified by electrostatic simulations. We are also introducing, for the first time, the mini-stopband-based cavity openings and their use to improve electron transport through the 2DEG.

To coherently transfer the information from a photonic-qubit to a singlet-triplet-spin-qubit in a GDQD, entanglement between the photoexcited electron and hole must be eliminated. As reported in detail by Joecker *et al.* [20], one possible transfer protocol is described by:

$$\begin{aligned} |\uparrow\circ\rangle|\omega_1, V\rangle &\xrightarrow{\text{photoexc.}} |\uparrow\circ\rangle|\downarrow\uparrow\rangle \xrightarrow{\text{adiabatic transfer}} |T_0\rangle|\circ\uparrow\rangle \\ |\uparrow\circ\rangle|\omega_2, V\rangle &\xrightarrow{\text{photoexc.}} |\uparrow\circ\rangle|\uparrow\downarrow\rangle \xrightarrow{\text{Rabi + ad. transf.}} |S\rangle|\circ\uparrow\rangle, \end{aligned} \quad (1)$$

where the bra-ket on the left- and right-hand side stands for the occupation of the GDQD and OAQD, respectively; an electron and hole spin is represented by a single and double arrow, respectively. The energy of the incident photon is described by the frequency $\omega_{1/2}$, and the vertical and horizontal polarization by V and H , respectively. Polarization is defined relative to the orientation of the magnetic field that is externally applied along a direction within the plane of the quantum well. Vertical and horizontal indicate that the polarization, which is always parallel to the quantum well, is perpendicular and parallel to the magnetic field, respectively. The transfer process consists of two steps:

- (i) Creation of a bound exciton in the OAQD by the absorption of the incident photon in the Voigt configuration, i.e., in the presence of a strong in-plane magnetic field.
- (ii) Adiabatic transfer of the photoexcited electron into the GDQD. Coherent transfer of the electron between the OAQD and the GDQD is achieved by adiabatically increasing the detuning between the electronic levels in the two systems. Additionally, a Rabi pulse is utilized to modulate the detuning to establish the singlet state.

By means of the transfer protocol, photonic states with different energies (but the same vertical polarization) are coherently transferred to a singlet-triplet spin state, wherein the spin-dependent energy of the exciton in the presence of an external magnetic field arises from the different g -factors of electrons and holes. This protocol was estimated to be completed with a fidelity of 84% for a singlet-triplet-spin-qubit [20], assuming that the capture of the incident photon is successful, and a bound exciton is created in the OAQD. Therefore, increasing the conversion efficiency between the photon and the bound exciton

is another important aspect, which is the main topic of this paper.

In the original model proposed by Joecker *et al.* [20], an InAs SAQD was assumed to be the OAQD. In this paper, we instead implement the OAQD as a gate-defined exciton trap. This is advantageous due to the improved fabrication scalability and the enhanced tunability of the exciton energy and associated emission wavelength afforded by the QCSE. Moreover, the electrically controllable tunnel coupling strength between the gate-defined exciton trap and the GDQD provides us with more flexibility to operate the device in view of achieving optimal transfer fidelity. On the other hand, the additional metal gate required for the OAQD introduces extra optical absorption, which reduces the overall photon extraction efficiency by 30% relative to what would otherwise be achievable with the remaining electrode system.

The protocol can be inverted, i.e., starting from a singlet-triplet-spin qubit and transferring the quantum information to an energy-encoded photon emitted from the OAQD and collected by a single-mode fiber. In this paper, we also focus on this reverse scheme since it could be more simply simulated with the available numerical tools, but conclusions apply to both processes due to reciprocity.

III. OPTICAL INTERFACE ASSISTED BY A PHOTONIC CRYSTAL CAVITY

Figure 2(a) presents the schematic overview of our optical interface. To efficiently couple the emitted photon to a single-mode fiber, we positioned the OAQD at the center of a carefully designed 2D PCC. The triangular lattice of holes is etched through the GaAs/(Al,Ga)As heterostructure membrane. Four cavity openings are integrated into the PCC to facilitate electron transport, as required by the quantum dot charge sensor and the GDQD, without compromising optical confinement at the target wavelength (i.e., 823 nm). Routing of the Au/Ti wires required for the application of the electrostatic potentials and the control pulses through the photonic crystal necessitates a high alignment accuracy of <15 nm between the PCC and the metallic wires in an electron beam lithography process, considering the width of the wires and the distance between adjacent holes. As demonstrated by our first fabrication attempts [43] and by experiments reported by other research groups [44,45], the desired accuracy level can be achieved. A 200-nm-thick gold reflector [not shown in Fig. 2(a)] is positioned at 305 nm below the GaAs quantum well layer to recycle photons emitted downward. The space between the gold reflector and the GaAs/(Al,Ga)As membrane is filled with a SiO₂ interlayer. The reflector position is optimized to maximize the extraction efficiency and ensure a high optical overlap of the far-field emission pattern with an ideal Gaussian beam propagating perpendicular to the membrane in the positive z -direction.

In addition to enhancing the central lobe of the far-field emission of the PCC, the reflector also suppresses side lobes, increasing the purity of the emitted Gaussian beam [39].

We designed the PCC by modifying a hexagonal H4 cavity [39], with a lattice constant $a_1 = 290$ nm and a hole radius $r_1 = 109$ nm [Fig. 2(a)]. Those parameters ensured that a transverse electrical (TE) photonic bandgap opens from 717 to 1021 nm for a vacuum-suspended planar lattice etched onto the GaAs/(Al,Ga)As membrane. We removed the holes marked in red in Fig. 2(b) for two reasons. First, this simplifies the routing of metal wires and allows for optimal positioning to minimize optical absorption. Second, the openings in the diagonal directions enable a continuous 2DEG within that region of the quantum well, which is essential for the functionality of the quantum dot charge sensor and the GDQD. The trapped surface charges on the side walls of the etched holes deplete the free carriers in their vicinity, so that electron transport is otherwise suppressed in the regular photonic crystal lattice. We measured the electrical resistance between two Ohmic contacts blocked by a comparable number of layers of unpassivated holes, with the same lattice pitch and hole radius as the photonic crystal in Fig. 2(a), to be around $1\text{ M}\Omega$ (see Supplemental Material [46]). However, this resistance drops to around $4\text{ k}\Omega$ if an opening similar to the cavity openings in Fig. 2(a) is created. This is sufficiently small not to additionally burden electron transport, given that the measured resistance already reaches several $\text{k}\Omega$ before etching the PCC. In addition to cavity openings, surface passivation techniques [47,48] can also be applied to reduce surface charge accumulation, further facilitating electrical transport and reducing electrostatic interaction with the exciton, spin-qubit, and charge sensor.

On the other hand, the cavity openings supported undesired photonic crystal waveguide modes, which destroyed the optical confinement of the PCC. We remedied this issue by utilizing the mini stopband of the so-formed photonic crystal waveguides [40], which is a result of the anticrossing of different waveguide modes with the same symmetry. According to our simulations, such a mini stopband opens from 1030 to 1058 nm after the removal of the red holes in Fig. 2(b). In order to shift the mini stopband to the working wavelength of the OAQD, the holes marked in blue in Fig. 2(b) are downscaled to a lattice pitch $a_2 = a_3 = 214$ nm, as indicated by the blue and purple circles in Figs. 2(c) and 2(d). The downscaled holes have a radius of $r_2 = 73$ nm (marked in blue), while the holes closest to the openings (marked in purple) have an increased radius of $r_3 = 90$ nm. This last modification allows for a wider mini stopband without burdening the fabrication process further. Figure 2(e) shows the TE band structure calculated along the direction of the cavity opening. As we can see, the mini stopband is shifted to the

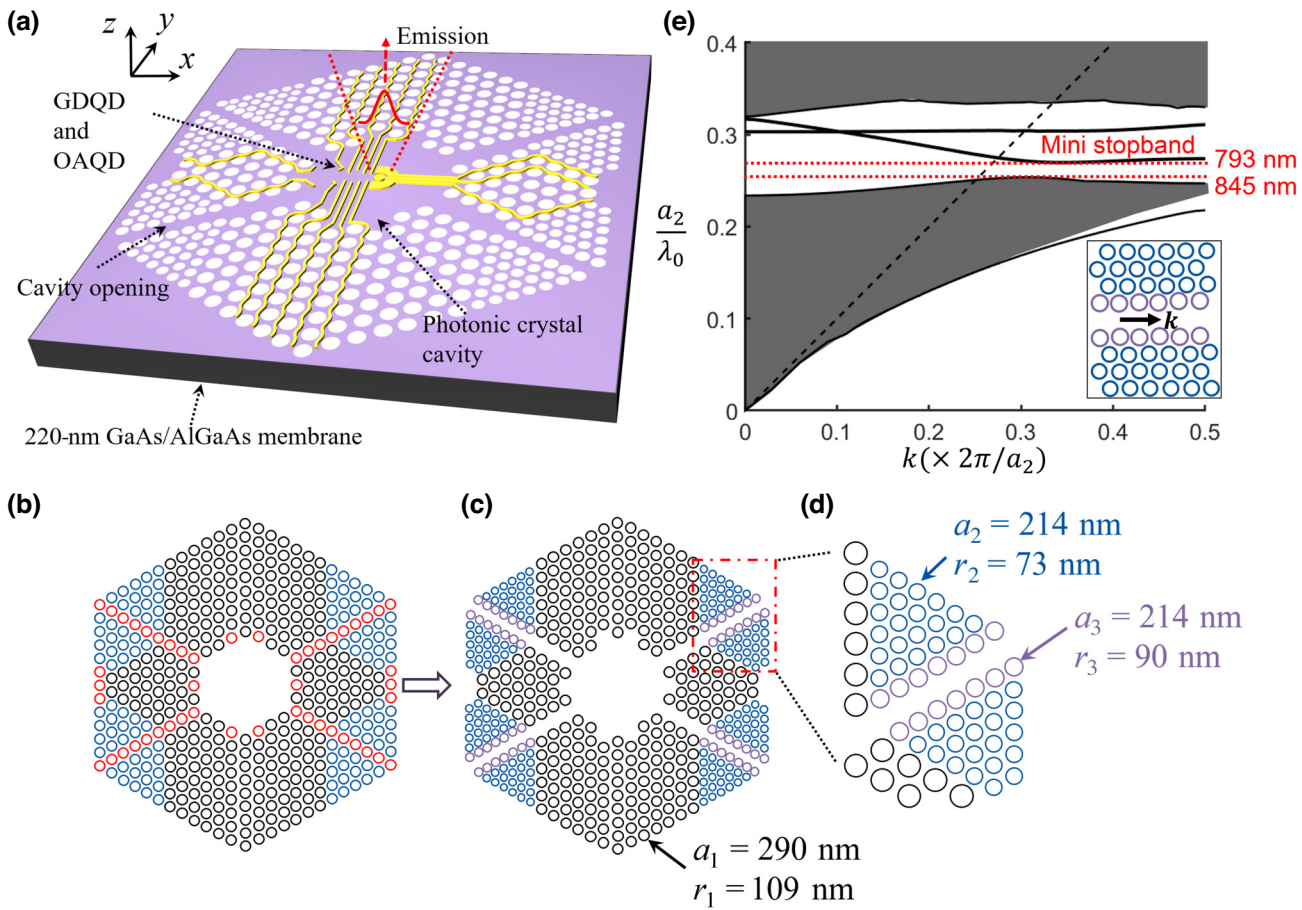


FIG. 2. (a) Schematic overview of the optical interface, including the photonic crystal cavity, the electrode system, and the cavity openings forming unwanted photonic crystal waveguides in which light propagation is blocked by a mini stopband. A 200-nm-thick gold reflector (not shown) is attached to the membrane via a SiO₂ interlayer, whose thickness is optimized to coherently recycle photons emitted downward. (b) Schematic view of a complete triangular H4 cavity. The holes marked by red circles are removed, while the holes shown in blue are downscaled to move the mini stopbands to the target wavelength. (c) Final cavity structure after the modification. (d) Detailed view of the lattice around the openings. The holes immediately adjacent to the openings have an enlarged radius in order to achieve a wider mini stopband. (e) Calculated band structure of the cavity opening from (d). The dashed black line indicates the light line in a vacuum. A mini stopband opens from $\lambda_0 = 793 \text{ nm}$ to $\lambda_0 = 845 \text{ nm}$. The inset shows the calculated structure and the direction of the in-plane wave vector.

wavelength range from 793 to 845 nm with an increased spectral width of 52 nm. The shaded areas represent the extended modes in the downscaled crystal (lattice constant a_2 and hole radius r_2). The guided waveguide modes are indicated by the black solid lines. The OAQD's working wavelength (i.e., 823 nm) falls within the center of this mini stopband, achieved through parameter optimization for rapid decay of the electromagnetic field along the openings.

We performed three-dimensional finite-difference time-domain (3D FDTD) simulations to evaluate the theoretical performance of the complete structure by using a commercially available software package (Lumerical FDTD). We model the exciton by an in-plane dipole since its hole is predominantly of a heavy-hole type for the lowest energy valence subband. This is not entirely exact, as quantum

wells induce some level of heavy-hole to light-hole mixing that can result in an off-plane polarization component. However, light emission with an in-plane (TE) polarization is further enhanced by the Purcell effect associated with the PCC. This is not the case for transverse magnetic (TM) emission, as the photonic crystal lattice does not feature a full TM bandgap. As a result, potential heavy-hole light-hole mixing is not expected to play a significant role here. Within the plane of the chip surface, the polarization of the photon emitted by the OAQD by pure excitonic states is further determined by the orientation of the in-plane magnetic field in the Voigt configuration, as a consequence of the resulting exciton state energy splitting. Thus, we model the OAQD by an electric dipole oriented in the y -direction (V) with the in-plane magnetic field oriented along the x -direction.

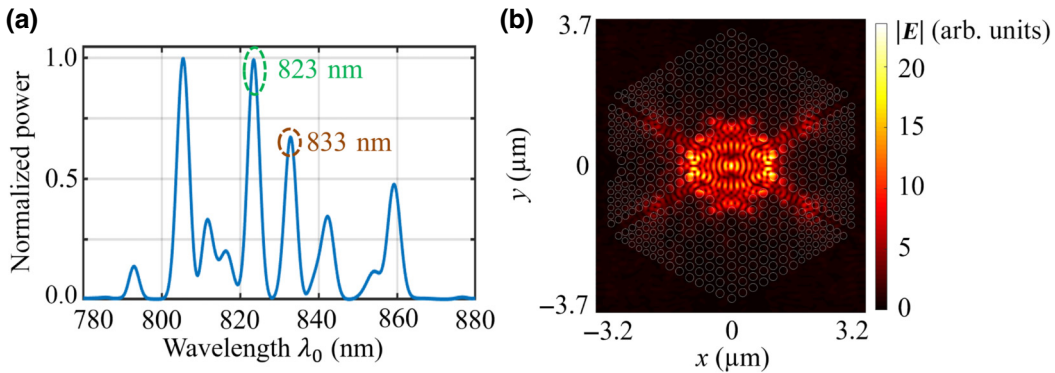


FIG. 3. (a) Normalized cavity power spectrum from 780 to 880 nm obtained from a cavity ring-down simulation. The target mode, which has a high extraction efficiency, is marked by a green dashed circle at 823 nm. For comparison to the target mode, another cavity mode at 833 nm is also highlighted by a brown circle. (b) Real space cavity mode profile of the 823 nm target mode excited by a y -directed dipole. An exponentially decaying electric field is observed along the cavity openings as a consequence of the mini stopband.

The bandgap energies of GaAs and $\text{Al}_{0.33}\text{Ga}_{0.67}\text{As}$ under liquid helium cryogenic temperature (4 K) are $E_{4\text{K},\text{GaAs}} = 1.52$ eV and $E_{4\text{K},(\text{Al},\text{Ga})\text{As}} = 1.90$ eV [49], corresponding to optical transition wavelengths of 816 and 652 nm, respectively. Consequently, $\text{Al}_{0.33}\text{Ga}_{0.67}\text{As}$ is fully transparent at 823 nm, while GaAs exhibits weak absorption at this wavelength due to the Urbach tail [50] and exciton absorption near the band edge. However, as our 220-nm membrane structure has a small GaAs fraction (i.e., two cap layers of 10 nm and a quantum well layer of 20 nm), we modeled the GaAs layers as lossless for simplicity. The refractive indices of GaAs and $\text{Al}_{0.33}\text{Ga}_{0.67}\text{As}$ are estimated to be $n_{4\text{K},\text{GaAs}} = 3.59$ and $n_{4\text{K},(\text{Al},\text{Ga})\text{As}} = 3.38$ at 823 nm at 4 K, respectively, considering their temperature dependences [51] and linearly extrapolating them. The inaccuracy in the assumed refractive indices introduced by the linear extrapolation will be addressed by experimental iterations. For the SiO_2 interlayer, we used an index of $n_{\text{SiO}_2} = 1.45$.

The cavity power spectrum obtained from a cavity ring-down simulation is presented in Fig. 3(a) from 780 to 880 nm. The cavity is excited by an electric dipole oriented along the y -direction and located at the center of the cavity, which corresponds to the position of the OAQD. Due to the large size of the cavity, chosen to minimize electrostatic interaction between the quantum dots and surface charges at the etched holes, multiple resonant peaks are observed. The target mode at 823 nm is specifically highlighted with a dashed green circle. The parameters of the PCC, including the lattice constants and hole radii, are carefully engineered to ensure that the wavelength of this target mode coincides with the working wavelength of the OAQD at 823 nm.

In Fig. 3(b), the cavity field profile at 823 nm is plotted in the plane of the PCC. It is evident that the optical confinement is effectively maintained, thanks to the presence of the mini stopband. The electromagnetic field decays

exponentially as it propagates along the openings. This feature is essential for guiding the emitted photons upward.

Pronounced vertical radiation is achieved for the target mode at 823 nm. Figure 4(a) shows the projected electrical field intensity at a distance of 1 m from the membrane, obtained by decomposing the near field into a series of plane waves and applying a far-field transform. The targeted single-beam vertical emission is observed, clearly indicated by the pronounced far-field intensity peak at $x = 0$ and $y = 0$. The 200-nm-thick gold reflector is positioned 305 nm below the OAQD, which corresponds to a SiO_2 interlayer thickness of 195 nm. The reflector position is optimized to facilitate constructive interference and enhance the central emission peak while simultaneously suppressing the side lobes [39].

The pronounced vertical emission observed in the target mode is a result of Bragg scattering caused by the periodic lattice of the PCC. Figure 4(b) shows the cavity mode profile in Fourier space for the target mode. For a triangular lattice, the reciprocal lattice (white dots) is spanned by two primitive lattice vectors, meaning that

$$\vec{V}_1 = \frac{2\pi}{a_1} \hat{\mathbf{e}}_y + \frac{2\pi}{\sqrt{3}a_1} \hat{\mathbf{e}}_x, \quad \vec{V}_2 = \frac{2\pi}{a_1} \hat{\mathbf{e}}_y - \frac{2\pi}{\sqrt{3}a_1} \hat{\mathbf{e}}_x, \quad (2)$$

where $a_1 = 290$ nm is the lattice constant of the PCC and $\hat{\mathbf{e}}_x$ and $\hat{\mathbf{e}}_y$ are unit vectors in reciprocal space. The target mode exhibits dominant k -space components around the reciprocal lattice points at $\pm(\vec{V}_1 - \vec{V}_2)$, which form a standing wave along the x -direction. Enhanced vertical emission is, therefore, achieved through Bragg scattering of these dominant k -space components to the Γ -point ($k_x = k_y = 0$). Additionally, standing waves along the directions of the cavity openings are clearly visible in Fig. 4(b).

For comparison to the pronounced vertical emission observed from the target mode at 823 nm, the far-field

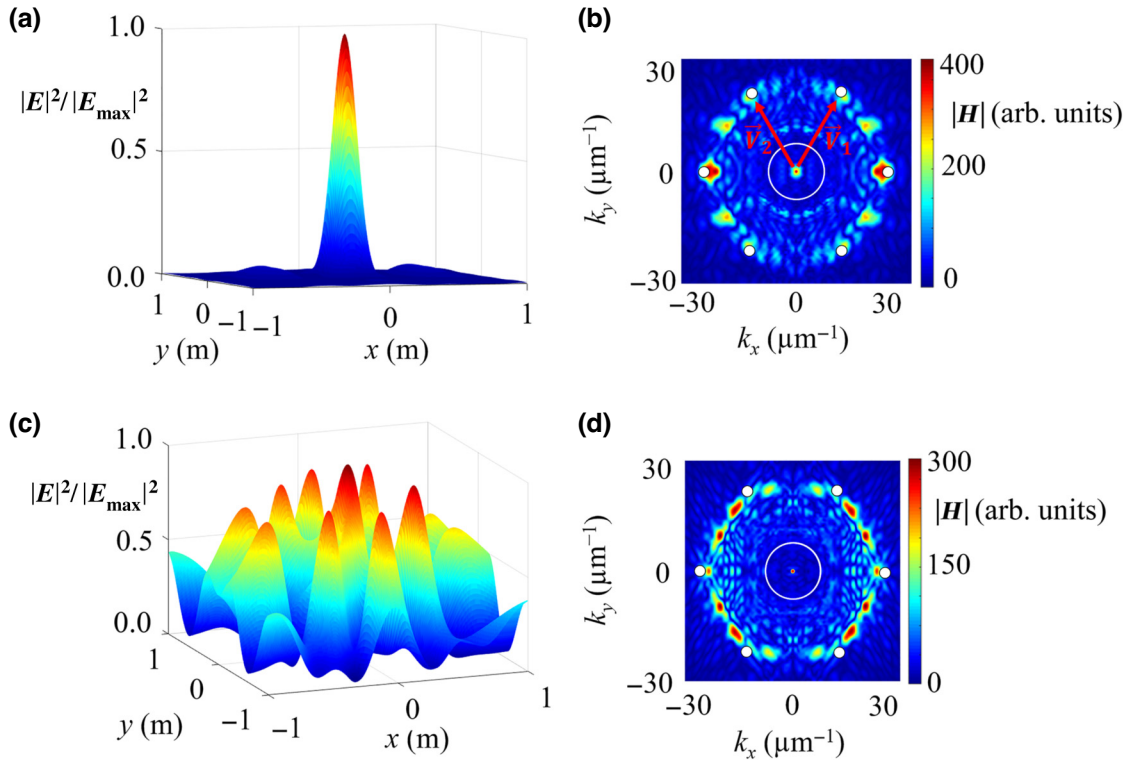


FIG. 4. (a) Far-field pattern at 823 nm calculated on a plane parallel to the membrane surface. The plane has a size of 2 m by 2 m in the x - and y -direction and is located at a distance $z = 1$ m from the OAQD ($x, y, z = 0$). Vertical emission with a pronounced Gaussian shape is observed. (b) Fourier space distribution of the target PCC mode. The red arrows indicate the primitive reciprocal lattice vectors and the white circle represents the light line in free space. The dominant k -space components are located around the reciprocal lattice points at $\pm(\vec{V}_1 - \vec{V}_2)$, which results in the enhanced vertical emission. (c) Far-field pattern at 833 nm, with the other mode marked in Fig. 3(a) for comparison. The complex pattern is very different from a Gaussian beam profile. Note that the far-field patterns are independently normalized in (a),(c). (d) Fourier space distribution of the PCC mode at 833 nm. The dominant field components do not coincide with the reciprocal lattice points.

emission pattern and the k -space profile of the 833 nm cavity mode are depicted in Figs. 4(c) and 4(d). We can clearly see that the dominant field components of this mode are not at the reciprocal lattice points of the PCC and, thus, cannot become efficiently coupled to the Γ -point. This results in the complex far-field emission pattern observed in Fig. 4(c), which couples poorly to a single-mode fiber.

To calculate the probability of photons emitted by the OAQD coupling into a single-mode fiber, we apply the following method. First, the electromagnetic field is recorded by a 2D monitor parallel to the membrane, with dimensions of 5 μm by 5 μm and located at a vertical distance of $z = 130$ nm above the OAQD in free space (i.e., 20 nm above the upper surface of the membrane). The electro-

magnetic power P_r is calculated by integrating the normal component of the Poynting vector over the entire monitor surface. We define the radiation efficiency as follows:

$$\eta_r = \frac{P_r}{P_{\text{dipole}}}, \quad (3)$$

which represents the fraction of dipole power P_{dipole} that is transmitted through the monitor surface P_r . This radiation efficiency η_r corresponds to the probability that the photons emitted by the OAQD escape the membrane via the top surface and propagate into free space.

Next, we calculate the optical overlap (O_V) between the electromagnetic field recorded by the monitor and an ideal Gaussian beam using the formula [52]:

$$O_V(\theta) = \frac{\iint (\vec{E}_m \times \vec{H}_g^*(\theta) + \vec{E}_g^*(\theta) \times \vec{H}_m) \cdot d\vec{S} |^2}{4 \iint \text{Re}(\vec{E}_m \times \vec{H}_m^*) \cdot d\vec{S} \iint \text{Re}(\vec{E}_g(\theta) \times \vec{H}_g^*(\theta)) \cdot d\vec{S}}. \quad (4)$$

Here, \vec{E}_m and \vec{H}_m are the electric and magnetic field recorded by the monitor, respectively, and $\vec{E}_g(\theta)$ and $\vec{H}_g(\theta)$ represent the electric and magnetic field of a linearly polarized Gaussian beam with a $1/e^2$ intensity half angle θ , respectively. To generate the Gaussian beam numerically, we construct a series of plane waves in momentum space, which consider the Gaussian amplitude distribution and their polarization relative to the dipole moment oriented in the y -direction. We then apply an inverse Fourier transform to calculate the real space beam profile. The spatial position of the Gaussian beam is optimized separately to maximize O_V .

Finally, we define the overall efficiency of our optical interface as follows:

$$\eta(\theta) = \eta_r O_V(\theta), \quad (5)$$

which is equal to the probability that the emitted photons couple into a free-space Gaussian beam with a divergence angle θ , which can be simply coupled to the fundamental mode of a single-mode fiber with the help of a lens system.

The values of O_V and $\eta(\theta)$ are calculated for the two cavity modes highlighted in Fig. 3(a) at 823 and 833 nm and plotted in Fig. 5. For the 823 nm target mode, a maximum optical overlap ($O_{V\max}$) of 0.526 is achieved at a small divergence angle of 10° due to the pronounced vertical emission with a radiation efficiency of $\eta_r = 54.6\%$. As a result, the maximum overall efficiency (η_{\max}) is calculated as $\eta_{\max} = \eta_r O_{V\max} = 28.7\%$. On the other hand, the optical overlap curve for the 833 nm mode shows a continuous increase with the divergence angle up to the maximum investigated angle of 80° and stays below $O_{V\max} = 0.101$. This results in $\eta_{\max} = 3.8\%$ with $\eta_r = 37.2\%$. This mode lacks the pronounced vertical emission characteristic observed from the 823 nm mode, resulting in poor overall efficiencies even at higher divergence angles and serves to highlight the importance of careful cavity mode design.

To demonstrate the effectiveness of the PCC, we also calculate the overall efficiency when the PCC is removed, i.e., an unetched GaAs/(Al,Ga)As membrane with the same gate structure, SiO₂ interlayer, and gold reflector at the same distance. In this case, we obtain $O_{V\max} = 0.600$ for a divergence angle of 54° , slightly better than the PCC, but a much reduced overall value of $\eta_{\max} = 4.6\%$ resulting from the poor radiation efficiency of $\eta_r = 7.8\%$ in the absence of the PCC. The function of the PCC can, thus, be summarized as enhancing the radiation efficiency while, at the same time, maintaining a Gaussian emission profile. Moreover, since the PCC significantly reduces the divergence angle of the emitted Gaussian beam, an objective with a lower numerical aperture and, thus, with a longer working distance can be used down the line to pick up the beam, facilitating the experimental implementation.

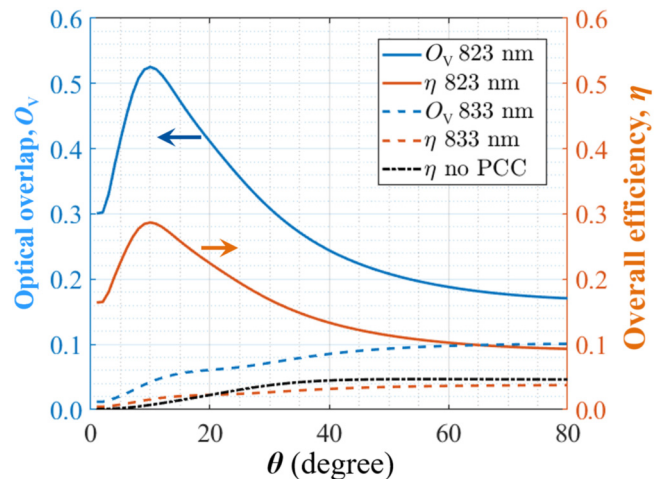


FIG. 5. Calculated O_V (blue curves) and overall efficiencies (orange curves) as a function of the divergence angle of a Gaussian beam for the two highlighted cavity modes at 823 nm (solid curves) and 833 nm (dashed curves). As a comparison, the overall efficiency without the PCC is also plotted (black dotted curve).

The PCC enhances the spontaneous emission of the dipole by a Purcell factor (relative to vacuum) of 2.19 for the targeted TE mode, compared with a Purcell factor of 0.74 (TE) in the absence of the PCC. The relatively low Purcell factor can be explained by the relatively large modal volume and the low-quality factor (below 300) of the H4 cavity. Moreover, the PCC also suppresses light-hole emission with a Purcell factor of 0.67 for the TM mode at 823 nm, which suggests that the heavy-hole light-hole mixing does not play a significant role and confirms that the polarization of the emission is predominantly in the plane.

Figure 6(a) presents a comparison of the calculated O_V and η for the PCC structure with and without the SiO₂ interlayer. The suspended PCC structure (without the interlayer), which could be fabricated by undercutting the SiO₂ in a final fabrication step, is represented by the dashed curves, while the PCC with the SiO₂ interlayer is depicted by the solid curves. In both cases, the distance between the gold reflector and the GaAs quantum well layer is optimized to achieve constructive interferences for the central Gaussian peak, with distances of 305 and 410 nm from the quantum well layer for the PCC with and without the interlayer, respectively. We see, in Fig. 6(a), that the maximum overlap $O_{V\max}$ is 0.525 and 0.839 with and without the interlayer, respectively, at the same divergence angle $\theta = 10^\circ$. The calculated radiation efficiency is $\eta_r = 54.6\%$ with the interlayer and $\eta_r = 57.8\%$ without the interlayer. Therefore, the maximum overall efficiencies with and without the interlayer are $\eta_{\max} = \eta_r O_{V\max} = 28.7\%$ and 48.5%, respectively. This comparison shows that the SiO₂ interlayer in the overall PCC structure leads to reduced O_V

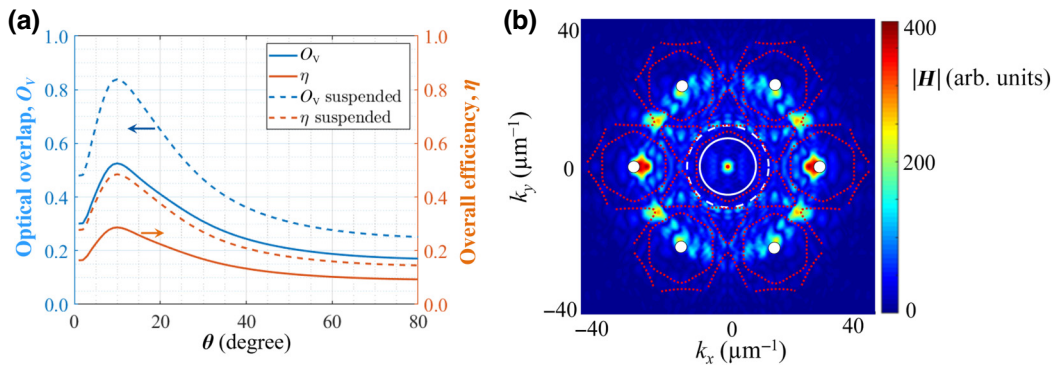


FIG. 6. (a) Calculated O_V and overall efficiency as a function of θ for the cavity mode at 823 nm. The reflector position is implicitly optimized for each case. In the presence of the SiO_2 interlayer, $O_{V\max}$ decreases from 0.839 to 0.526 and the η_{\max} from 48.5% to 28.7% at $\theta = 10^\circ$, as a consequence of the broken symmetry along the z -direction. (b) Fourier space distribution of the target TE-like cavity mode at 823 nm overlaid with the equifrequency contours of the leaky TM-like photonic crystal modes at the same wavelength. The light line of vacuum (SiO_2) is depicted by the white solid (dashed) circle, and the k -vectors of the TM-like photonic crystal modes are indicated by the red dotted contour. An overlap between the TE-like cavity mode field components and the TM-like photonic crystal modes is observed.

and η_r . This is due, on the one hand, to increased emission toward the reflector resulting from the decreased refractive index contrast. Additionally, the presence of the SiO_2 interlayer breaks the symmetry of the structure along the z -direction and induces coupling between the quasi-TE and quasi-TM modes [53]. Since the bandgap is open for the TE fields only, this contributes to the further reduction of the overall emission efficiency in the following ways.

The photonic crystal cavity ($a_1 = 290$ nm and $r_1 = 109$ nm) supports a TE bandgap from 717 to 1021 nm. Additionally, the cavity opening has a TE mini stopband from 793 to 845 nm, as illustrated in Fig. 2(e). Therefore, no TE mode propagating out of the cavity exists in the wavelength range from 793 to 845 nm and TE cavity modes are observed within the photonic crystal cavity. However, for the TM modes, such a bandgap does not exist. When the reflector symmetry is broken by the asymmetric SiO_2 interlayer in the z -direction and TE-TM coupling is possible, the TE-like cavity modes can couple into the TM-like propagating photonic crystal modes or the TM-like propagating waveguide modes and escape the cavity. This results in an additional in-plane loss inside the semiconductor membrane. Figure 6(b) shows the k -space profile of the target cavity mode together with the equifrequency contours of the TM-like photonic crystal modes at the same wavelength (i.e., 823 nm), represented by red dotted curves. The presence of field components on the equifrequency contours of the TM-like photonic crystal modes suggests the presence of in-plane TE-TM coupling loss.

By depositing an additional SiO_2 layer on top of the membrane, we are able to restore the mirror symmetry in the z -direction and, thus, suppress the TE-TM coupling. However, this also compromises the optical confinement by closing the optical bandgap of the photonic crystal and

the mini stopband of the cavity openings, which results in a reduced radiation efficiency and a lower optical overlap according to our simulations.

In addition to the TE-TM coupling loss, two other loss mechanisms (i.e., radiation losses via the bottom interface and optical absorption of the metal gates) also limit the performance of our optical interface. The gold reflector utilized in this setup reflects light traveling in the negative z -direction and efficiently enhances the Gaussian emission toward the top, which is emitted perpendicular to the chip surface. However, photons that are emitted at nonperpendicular angles to the surface of the reflector might experience multiple reflections that guide them along the 2D slab formed by the gold reflector and the GaAs/(Al,Ga)As membrane in the xy -plane. As a result, there is a possibility of radiation losses via the bottom semiconductor interface, which cannot be neglected. The light inside the SiO_2 light cone, but outside the vacuum light cone, remains guided. Moreover, even for the light within the vacuum light cone that eventually escapes the slab, this leads to a distortion of the emitted field profile, reducing the overlap O_V . Moreover, losses are introduced from multiple reflections from the metal mirror, which induces some absorption.

The optical absorption of the Au-Ti gates introduces another loss mechanism due to the presence of surface plasmon polaritons (SPP) at the metal-vacuum and metal- SiO_2 interfaces excited by the evanescent electromagnetic field of the target cavity mode. To reduce the SPP absorption, the gates and wires are predominantly routed along the y -direction to ensure that the metal-vacuum and metal- SiO_2 interfaces are mostly parallel to the dominant electric field component inside the cavity, which is E_y . The choice of this orientation is because the dominant electric field component of SPP modes is perpendicular to the metal-dielectric interface [54]. By routing the gates and

TABLE I. Calculated power ratio Γ and partial quality factors for each loss channel. Four different schemes are investigated: PCC with a SiO_2 interlayer and excited by a y -directed dipole, PCC with a SiO_2 interlayer and excited by an x -directed dipole, vacuum-suspended PCC excited by a y -directed dipole, and vacuum-suspended PCC excited by an x -directed dipole. The distance between the reflector and the GaAs/(Al,Ga)As membrane is optimized independently for all four cases. The polarization of the Gaussian beam used for calculating the O_V is always in the direction of the dipole moment.

	Q_{total}	$\Gamma_{\text{gates}}/Q_{\text{gates}}$	$\Gamma_{\text{TE-TM}}/Q_{\text{TE-TM}}$	$\Gamma_{\text{bottom}}/Q_{\text{bottom}}$	η_r/Q_{top}	$O_V \text{ max}$	η_{max}
SiO_2 y -directed dipole	232	25.8%/899	3.5%/6620	15.9%/1456	54.7%/424	0.526	28.7%
SiO_2 x -directed dipole	161	30.9%/521	6.6%/2426	22.5%/716	39.4%/409	0.347	13.7%
Suspended y -directed dipole	293	34.4%/851	1.4%/20285	5.9%/4996	57.8%/507	0.839	48.5%
Suspended x -directed dipole	236	42.5%/555	2.3%/10301	7.8%/3026	46.3%/510	0.719	33.3%

wires in this manner, the interaction between the SPP and the cavity mode is reduced, leading to decreased optical absorption.

To identify the dominant loss mechanisms and their dependency on polarization and cladding materials, we calculate the quality factors (Q) of the PCC structure by exciting the cavity with an x - or y -directed dipole at the position of the OAQD and recording the cavity spectrum with and without the SiO_2 interlayer. The results are summarized in Table I. The overall Q_{total} is evaluated by fitting the resonance peak via a Lorentzian curve and calculating the full width half maximum (FWHM). We also evaluate the ratio Γ of the lost power to the total power emitted by the dipole for the different loss channels and convert this result into the corresponding partial quality factors due to gates absorption (Γ_{gates} and Q_{gates}), TE-TM coupling loss ($\Gamma_{\text{TE-TM}}$ and $Q_{\text{TE-TM}}$), downward radiation (Γ_{bottom} and Q_{bottom}), and upward radiation (η_r and Q_{top}). The formulas for calculating Γ_{partial} and Q_{partial} are given as follows:

$$\Gamma_{\text{partial}} = \frac{P_{\text{partial}}}{P_{\text{dipole}}}, Q_{\text{partial}} = \frac{Q_{\text{total}}}{\Gamma_{\text{partial}}}, \quad (6)$$

where “partial” stands for “gates”, “TE-TM”, “bottom”, and “top”. Moreover, P_{dipole} is the power emitted by the dipole source, P_{gates} is the power absorbed by the gates, and $P_{\text{TE-TM}}$, P_{bottom} , and P_{top} are the power radiated to the side, bottom and top of the cavity, respectively. The power monitors used to record P_{bottom} and P_{top} are located in the vicinity of the bottom and top surfaces of the membrane and form a box with the power monitors used to record $P_{\text{TE-TM}}$, so that the latter corresponds to power escaping the photonic crystal within the membrane. Note that we use the already introduced radiation efficiency η , instead of the notation Γ_{top} to represent the ratio of the power emitted through the top interface. A high emission efficiency corresponding to a large η_r is obtained if Q_{top} is substantially lower than all the other partial Q -factors, which correspond to unwanted loss channels.

We see from Table I that the partial quality factor of the metal gates (Q_{gates}) is highly dependent on the dipole orientation. For an x -directed dipole, Q_{gates} is calculated as

521 and 555 with and without the SiO_2 interlayer, respectively. In contrast, the same Q_{gates} increases to 899 and 851 for a y -directed dipole, respectively, due to the reduced SPP absorption as a result of the optimized gate geometry. This confirms our assumption that routing the wires parallel to the dominant E -field component E_y reduces the corresponding absorption losses. This was further verified by evaluating one-by-one the absorption losses for each electrode, wherein it was found that the sensor and OAQD trap and guard electrodes, which had to be routed along the x -direction, induced most of the absorption losses.

As expected, $Q_{\text{TE-TM}}$ is significantly correlated to the presence or absence of the interlayer. When a SiO_2 interlayer is used, $Q_{\text{TE-TM}}$ is reduced by one order of magnitude due to the increased TE-TM coupling loss. Interestingly, even for a suspended PCC structure, there is still a slight but nonnegligible TE-TM coupling loss (with a power ratio of 1.4% for the y -directed dipole and 2.3% for the x -directed dipole excitation), which is possible since the gates also break the symmetry in the z -direction, as the GDQD is only patterned on the top semiconductor interface.

The power loss via the bottom interface is also increased when a SiO_2 interlayer is present because the reduced refractive index contrast enhances the downward emission and, thus, the amount of power lost due to the absorption by the metal reflector. Downward emitted light can also undergo multiple reflections between the reflector and the bottom surface of the membrane, leading to its lateral escape.

We notice that Q_{top} is around 500 for a suspended structure and around 400 for the case of an interlayer. The drop of Q_{top} when the interlayer is present is also expected due to the increased downward emission, since the part of the field that is reflected upward and escapes through the top surface is accounted for by Q_{top} . This reduction of Q_{top} in the presence of the interlayer is helpful as it makes the targeted loss channel compete more favorably with the other ones. However, the drop in Q_{top} is not sufficient to compensate for the drop of the other partial Q -factors, as seen in the reduced radiation efficiency. The dipole orientation has minimal influence on Q_{top} , as expected.

Table I also includes the calculation results for the maximum optical overlap ($O_{V\max}$) in all four schemes. We notice a pronounced correlation between $O_{V\max}$ and Q_{bottom} , which may be explained by multiple reflections and partial guiding in the underlying interlayer being applied to the downward emission before it escapes the structure through the top, distorting the emission profile. Based on these observations, the undercutting of the membrane appears desirable from a performance perspective, even though it increases the complexity of the fabrication process.

In the Supplemental Material [46], we also analyze the influence of fabrication imperfections, including the deviation of the hole radius and nonvertical side wall angles.

IV. CONCLUSION

In this paper, we present and numerically analyze the extraction efficiency of an optical interface between a singlet-triplet-spin-qubit and a photonic-qubit, including the GDQD, the OAQD, a charge sensor, and the photonic crystal cavity structure. The entire structure can be fully lithographically defined and deterministically fabricated, which greatly increases the scalability of on-chip integration. The photonic crystal cavity is designed such that the dominant wave vectors of the cavity mode at the working wavelength of the OAQD coincide with the reciprocal lattice vectors of the photonic crystal. As a result of strong Bragg scattering, we obtain enhanced vertical emission with a pronounced central lobe. According to our calculations, our design reaches a radiation efficiency of 54.7% and an optical overlap of 0.526 with a narrow Gaussian beam compatible with low numerical aperture collection optics. As a result, we expect an overall efficiency of 28.7%. The performance can be further increased by removing the SiO_2 interlayer between the semiconductor membrane and the gold reflector. In this case, the overall efficiency is estimated to be 48.5% with an optical overlap equal to 0.839 and a radiation efficiency of 57.8%.

ACKNOWLEDGMENT

This project is funded by the Deutsche Forschungsgemeinschaft (DFG, German Research Foundation) under Germany's Excellence Strategy – Cluster of Excellence Matter and Light for Quantum Computing (ML4Q) EXC 2004/1–390534769.

- [1] H. J. Kimble, The quantum internet, *Nature* **453**, 1023 (2008).
- [2] N. Gisin and R. Thew, Quantum communication, *Nat. Photonics* **1**, 165 (2007).

- [3] N. Gisin, G. Ribordy, W. Tittel, and H. Zbinden, Quantum cryptography, *Rev. Mod. Phys.* **74**, 145 (2002).
- [4] Liang Jiang, Jacob M. Taylor, Anders S. Sørensen, and D. Mikhail, Lukin “Distributed quantum computation based on small quantum registers”, *Phys. Rev. A* **76**, 062323 (2007).
- [5] Pascal Cerdantaine, Tim Botzem, Julian Ritzmann, Simon Sebastian Humpohl, Arne Ludwig, Dieter Schuh, Dominique Bougeard, Andreas D. Wieck, and Hendrik Bluhm, Closed-loop control of a GaAs-based singlet-triplet spin qubit with 99.5% gate fidelity and low leakage, *Nat. Commun.* **11**, 4144 (2020).
- [6] P. Cerdantaine, T. Botzem, D. P. DiVincenzo, and H. Bluhm, High-fidelity single-qubit gates for two-electron spin qubits in GaAs, *Phys. Rev. Lett.* **113**, 150501 (2014).
- [7] D. Riedel, I. Söllner, B. J. Shields, S. Starosielec, P. Appel, E. Neu, P. Maletinsky, and R. J. Warburton, Deterministic enhancement of coherent photon generation from a nitrogen-vacancy center in ultrapure diamond, *Phys. Rev. X* **7**, 031040 (2017).
- [8] Y. Chu, N. P. de Leon, B. J. Shields, B. Hausmann, R. Evans, E. Togan, M. J. Burek, M. Markham, A. Stacey, A. S. Zibrov, A. Yacoby, D. J. Twitchen, M. Lončar, H. Park, P. Maletinsky, and M. D. Lukin, Coherent optical transitions in implanted nitrogen vacancy centers, *Nano Lett.* **14**, 1982 (2014).
- [9] D. Englund, B. Shields, K. Rivoire, F. Hatami, J. Vučković, H. Park, and M. D. Lukin, Deterministic coupling of a single nitrogen vacancy center to a photonic crystal cavity, *Nano Lett.* **10**, 3922 (2010).
- [10] Tim Schröder, Sara L. Mouradian, Jiabao Zheng, Matthew E. Trusheim, Michael Walsh, Edward H. Chen, Luozhou Li, Igal Bayn, and Dirk Englund, Quantum nanophotonics in diamond, *J. Opt. Soc. Am. B* **33**, B65 (2016).
- [11] L.-M. Duan and C. Monroe, Colloquium: Quantum networks with trapped ions, *Rev. Mod. Phys.* **82**, 1209 (2010).
- [12] J. R. Petta, A. C. Johnson, J. M. Taylor, E. A. Laird, A. Yacoby, M. D. Lukin, C. Marcus, M. P. Hanson, and A. C. Gossard, Coherent manipulation of coupled electron spins in semiconductor quantum dots, *Science* **309**, 2180 (2005).
- [13] J. Elzerman, R. Hanson, J. S. Greidanus, L. H. Willems van Beveren, S. De Franceschi, L. M. K. Vandersypen, S. Tarucha, and L. P. Kouwenhoven, Few-electron quantum dot circuit with integrated charge read out, *Phys. Rev. B* **67**, 161308(R) (2003).
- [14] J. M. Elzerman, R. Hanson, L. H. Willems van Beveren, B. Witkamp, L. M. K. Vandersypen, and L. P. Kouwenhoven, Single-shot read-out of an individual electron spin in a quantum dot, *Nature* **430**, 431 (2004).
- [15] Hendrik Bluhm, Sandra Foletti, Izhar Neder, Mark Rudner, Diana Mahalu, Vladimir Umansky, and Amir Yacoby, Dephasing time of GaAs electron-spin qubits coupled to a nuclear bath exceeding 200 μ s, *Nat. Phys.* **7**, 109 (2011).
- [16] E. A. Chekhovich, M. N. Makhonin, A. I. Tartakovskii, A. Yacoby, H. Bluhm, K. C. Nowack, and L. M. K. Vandersypen, Nuclear spin effects in semiconductor quantum dots, *Nat. Mater.* **12**, 494 (2013).
- [17] Jun Yoneda, Kenta Takeda, Tomohiro Otsuka, Takashi Nakajima, Matthieu R. Delbecq, Giles Allison, Takumu Honda, Tetsuo Kodera, Shunri Oda, Yusuke Hoshi, Noritaka Usami, Kohei M. Itoh, and Seigo Tarucha, A

- quantum-dot spin qubit with coherence limited by charge noise and fidelity higher than 99.9%, *Nat. Nanotechnol.* **13**, 102 (2018).
- [18] J.-H. Kim, S. Aghaeimeibodi, C. J. K. Richardson, R. P. Leavitt, D. Englund, and E. Waks, Hybrid integration of solid-state quantum emitters on a silicon photonic chip, *Nano Lett.* **17**, 7394 (2017).
- [19] T. Descamps, F. Liu, S. Kindel, R. Otten, T. Hangleiter, C. Zhao, M. I. Lepsa, J. Ritzmann, A. Ludwig, A. D. Wieck, B. E. Kardynał, and H. Bluhm, Semiconductor membranes for electrostatic exciton trapping in optically addressable quantum transport devices, *Phys. Rev. Appl.* **19**, 044095 (2023).
- [20] B. Joecker, P. Cerfontaine, F. Haupt, L. R. Schreiber, B. E. Kardynał, and H. Bluhm, Transfer of a quantum state from a photonic qubit to a gate-defined quantum dot, *Phys. Rev. B* **99**, 205415 (2019).
- [21] X. Ding, Y. He, Z.-C. Duan, N. Gregersen, M.-C. Chen, S. Unsleber, S. Maier, C. Schneider, M. Kamp, S. Höfling, C.-Y. Lu, and J.-W. Pan, On-demand single photons with high extraction efficiency and near-unity indistinguishability from a resonantly driven quantum dot in a micropillar, *Phys. Rev. Lett.* **116**, 020401 (2016).
- [22] Julien Claudon, Joël Bleuse, Nitin Singh Malik, Maela Bazin, Pépine Jaffrennou, Niels Gregersen, Christophe Sauvan, Philippe Lalanne, and Jean-Michel Gérard, A highly efficient single-photon source based on a quantum dot in a photonic nanowire, *Nat. Photonics* **4**, 174 (2010).
- [23] A. Schleehahn, M. Gaafar, M. Vaupel, M. Gschrey, P. Schnauber, J.-H. Schulze, S. Rodt, A. Strittmatter, W. Stoltz, A. Rahimi-Iman, T. Heindel, M. Koch, and S. Reitzenstein, Single-photon emission at a rate of 143 MHz from a deterministic quantum-dot microlens triggered by a mode-locked external-cavity surface-emitting laser, *Appl. Phys. Lett.* **107**, 041105 (2015).
- [24] S. Fischbach, A. Kaganskiy, E. Burcu, Y. Tauscher, F. Gericke, A. Thoma, R. Schmidt, A. Strittmatter, T. Heindel, S. Rodt, and S. Reitzenstein, Efficient single-photon source based on a deterministically single quantum dot-microstructure with back side gold mirror, *Appl. Phys. Lett.* **111**, 011106 (2017).
- [25] Natasha Tomm, Alisa Javadi, Nadia Olympia Antoniadis, Daniel Najer, Matthias Christian Löbl, Alexander Rolf Korsch, Rüdiger Schott, Sascha René Valentin, Andreas Dirk Wieck, Arne Ludwig, and Richard John Warburton, A bright and fast source of coherent single photons, *Nat. Nanotechnol.* **16**, 399 (2021).
- [26] M. Davanço, M. T. Rakher, W. Wegscheider, D. Schuh, A. Badolato, and K. Srinivasan, Efficient quantum dot single photon extraction into an optical fiber using a nanophotonic directional coupler, *Appl. Phys. Lett.* **99**, 121101 (2011).
- [27] Raphaël S. Daveau, Krishna C. Balram, Tommaso Pernigotti, Jin Liu, Eun H. Lee, Jin D. Song, Varun Verma, Richard Mirin, Sae Woo Nam, Leonardo Midolo, Søren Stobbe, Kartik Srinivasan, and Peter Lodahl, Efficient fiber-coupled single-photon source based on quantum dots in a photonic-crystal waveguide, *Optica* **4**, 178 (2017).
- [28] Simon Gröblacher, Jeff T. Hill, Amir H. Safavi-Naeini, Jasper Chan, and Oskar Painter, Highly efficient coupling from an optical fiber to a nanoscale silicon optomechanical cavity, *Appl. Phys. Lett.* **103**, 181104 (2013).
- [29] Peter Lodahl, A. Floris van Driel, Ivan S. Nikolaev, Arie Irman, Karin Overgaag, Daniël Vanmaekelbergh, and Willem L. Vos, Controlling the dynamics of spontaneous emission from quantum dots by photonic crystals, *Nature* **430**, 654 (2004).
- [30] D. Englund, D. Fattal, E. Waks, G. Solomon, B. Zhang, T. Nakaoka, Y. Arakawa, Y. Yamamoto, and J. Vučković, Controlling the spontaneous emission rate of single quantum dots in a two-dimensional photonic crystal, *Phys. Rev. Lett.* **95**, 013904 (2005).
- [31] I. J. Luxmoore, R. Toro, O. Del Pozo-Zamudio, N. A. Wasley, E. A. Chekhovich, A. M. Sanchez, R. Beanland, A. M. Fox, M. S. Skolnick, H. Y. Liu, and A. I. Tartakovskii, III–V quantum light source and cavity-QED on silicon, *Sci. Rep.* **3**, 1239 (2013).
- [32] H. Kim, D. Sridharan, T. C. Shen, G. S. Solomon, and E. Waks, Strong coupling between two quantum dots and a photonic crystal cavity using magnetic field tuning, *Opt. Express* **19**, 2589 (2011).
- [33] Kazuhiro Kuruma, Yasutomo Ota, Masahiro Kakuda, Satoshi Iwamoto, and Yasuhiko Arakawa, Strong coupling between a single quantum dot and an L4/3 photonic crystal nanocavity, *Appl. Phys. Express* **13**, 082009 (2020).
- [34] Ravitej Uppu, Freja T. Pedersen, Ying Wang, Cecilie T. Olesen, Camille Papon, Xiaoyan Zhou, Leonardo Midolo, Sven Scholz, Andreas D. Wieck, Arne Ludwig, and Peter Lodahl, Scalable integrated single-photon source, *Sci. Adv.* **6**, eabc8268 (2020).
- [35] Nguyen-Vi-Quynh Tran, Sylvain Combrié, Pierre Colman, Alfredo De Rossi, and Ting Mei, Vertical high emission in photonic crystal nanocavities by band-folding design, *Phys. Rev. B* **82**, 075120 (2010).
- [36] Nguyen-Vi-Quynh Tran, Sylvain Combrié, and Alfredo De Rossi, Directive emission from high-Q photonic crystal cavities through band folding, *Phys. Rev. B* **79**, 041101(R) (2009).
- [37] T. Tajiri, Y. Sakai, K. Kuruma, S. M. Ji, H. Kiyama, A. Oiwa, J. Ritzmann, A. Ludwig, A. D. Wieck, Y. Ota, Y. Arakawa, and S. Iwamoto, Fabrication and optical characterization of photonic crystal nanocavities with electrodes for gate-defined quantum dots, *Jpn. J. Appl. Phys.* **59**, SGGI05 (2020).
- [38] Sangmin Ji, Takeyoshi Tajiri, Xiao-Fei Liu, Haruki Kiyama, Akira Oiwa, Julian Ritzmann, Arne Ludwig, Andreas D. Wieck and Satoshi Iwamoto, Polarization-independent enhancement of optical absorption in a GaAs quantum well embedded in an air-bridge bull's-eye cavity with metal electrodes, *Jpn. J. Appl. Phys.* **62**, SC1018 (2023).
- [39] K. Wu, B. Marzban, T. Descamps, H. Bluhm, F. Merget, and J. Witzenz, High-efficiency gate-defined quantum dot to single mode fiber interface assisted by a photonic crystal cavity, *AIP Adv.* **10**, 115016 (2020).
- [40] S. Olivier, H. Benisty, C. Weisbuch, C. J. M. Smith, T. F. Krauss, and R. Houdré, Coupled-mode theory and propagation losses in photonic crystal waveguides, *Opt. Express* **11**, 1490 (2003).
- [41] M. Lončar, D. Nedeljković, T. P. Pearsall, J. Vučković, A. Scherer, S. Kuchinsky, and D. C. Allan, Experimental and

- theoretical confirmation of Bloch-mode light propagation in planar photonic crystal waveguides, *Appl. Phys. Lett.* **80**, 1689 (2002).
- [42] G. J. Schinner, J. Repp, E. Schubert, A. K. Rai, D. Reuter, A. D. Wieck, A. O. Govorov, A. W. Holleitner, and J. P. Kotthaus, Confinement and interaction of single indirect excitons in a voltage-controlled trap formed inside double InGaAs quantum wells, *Phys. Rev. Lett.* **110**, 127403 (2013).
- [43] K. Wu, T. Descamps, B. Marzban, J. C. Müller, S. Kindel, M. Künne, F. Merget, H. Bluhm, J. Witzens, Highly efficient spin qubit to photon interface assisted by a photonic crystal cavity, *Proc. SPIE Int. Soc. Opt. Eng.* **11995**, 40 (2022).
- [44] Ch. Blömers, T. Grap, M. I. Lepsa, J. Moers, St. Trellenkamp, D. Grütmacher, H. Lüth, and Th. Schäpers, Hall effect measurements on InAs nanowires, *Appl. Phys. Lett.* **101**, 152106 (2012).
- [45] J. Moers, St. Trellenkamp, D. Grütmacher, A. Offenhäusser, and B. Rienks, Optimized marker definition for high overlay accuracy e-beam lithography, *Microelectron. Eng.* **97**, 68 (2012).
- [46] See Supplemental Material at <http://link.aps.org supplemental/10.1103/PhysRevApplied.21.054052> for the measurement of the resistance between Ohmic contacts blocked by photonic crystals with openings of varying dimensions and the analysis of fabrication tolerances based on FDTD simulations.
- [47] Biswarup Guha, Felix Marsault, Fabian Cadiz, Laurence Morgenroth, Vladimir Ulin, Vladimir Berkovitz, Aristide Lemaître, Carmen Gomez, Alberto Amo, Sylvain Combrié, Bruno Gérard, Giuseppe Leo, and Ivan Favero, Surface-enhanced gallium arsenide photonic resonator with quality factor of 6×10^6 , *Optica* **4**, 218 (2017).
- [48] Kazuhiro Kuruma, Yasutomo Ota, Masahiro Kakuda, Satoshi Iwamoto, and Yasuhiro Arakawa, Surface-passivated high- Q GaAs photonic crystal nanocavity with quantum dots, *APL Photonics* **5**, 046106 (2020).
- [49] S. A. Lourenço, I. F. L. Dias, J. L. Duarte, E. Laureto, E. A. Meneses, J. R. Leite, and I. Mazzaro, Temperature dependence of optical transitions in AlGaAs, *J. Appl. Phys.* **89**, 6159 (2001).
- [50] A. V. Lehmen, J. P. Heritage, J. E. Zucker, D. S. Chemla, and A. C. Gossard, in *International Quantum Electronics Conference* (1986), pp. paper MG6.
- [51] J. Talghader and J. S. Smith, Thermal dependence of the refractive index of GaAs and AlAs measured using semiconductor multilayer optical cavities, *Appl. Phys. Lett.* **66**, 335 (1995).
- [52] S. Romero-García, B. Shen, F. Merget, B. Marzban, and J. Witzens, Alignment tolerant couplers for silicon photonics, *IEEE J. Sel. Top. Quantum Electron.* **21**, 765 (2015).
- [53] Yoshinori Tanaka, Takashi Asano, Ranko Hatsuta, and Susumu Noda, Investigation of point-defect cavity formed in two-dimensional photonic crystal slab with one-sided dielectric cladding, *Appl. Phys. Lett.* **88**, 011112 (2006).
- [54] L. Novotny and B. Hecht, in *Principles of Nano-Optics* (Cambridge University Press, Cambridge, 2012), pp. 369–413, <https://www.cambridge.org/core/books/principles-of-nano optics/E884E5F4AA76DF179A1ECFD77436452>.